

Cell swelling, softening and invasion in a three-dimensional breast cancer model

Yu Long Han¹, Adrian F. Pegoraro^{2,3}, Hui Li^{4,5}, Kaifu Li⁶, Yuan Yuan³, Guoqiang Xu¹, Zichen Gu¹, Jiawei Sun¹, Yukun Hao¹, Satish Kumar Gupta¹, Yiwei Li¹, Wenhui Tang¹, Hua Kang⁶, Lianghong Teng⁶, Jeffrey J. Fredberg⁷ and Ming Guo^{1*}

Control of the structure and function of three-dimensional multicellular tissues depends critically on the spatial and temporal coordination of cellular physical properties, yet the organizational principles that govern these events and their disruption in disease remain poorly understood. Using a multicellular mammary cancer organoid model, we map here the spatial and temporal evolution of positions, motions and physical characteristics of individual cells in three dimensions. Compared with cells in the organoid core, cells at the organoid periphery and the invasive front are found to be systematically softer, larger and more dynamic. These mechanical changes are shown to arise from supracellular fluid flow through gap junctions, the suppression of which delays the transition to an invasive phenotype. These findings highlight the role of spatiotemporal coordination of cellular physical properties in tissue organization and disease progression.

Living cells are dynamic systems undergoing processes ranging from gene expression, intracellular dynamics and forces at the molecular level^{1–3} to cell contraction, deformation and migration at the cellular level^{4–10}. Within a multicellular tissue, the precise control of these physical characteristics in space and time is critical for the maintenance of mechanical integrity and biological function. Deviation from mechanical homeostasis is associated with diseases, including aberrant wound repair, developmental abnormalities and cancer^{11–17}. In isolated cells in vitro, for example, increased deformability^{18–21}, intracellular dynamics²², contractility²³ and mobility have each been identified as a physical hallmark of different types of cancer²⁴ and have been proposed as potential targets for cancer treatment²⁵. Despite the promise of in vitro approaches, extensive studies have shown that the mechanical properties of cells are regulated by their microenvironment, including but not limited to stiffness of the surrounding matrix, cell densities and dimensions^{26,27}. Hence, in the context of a multicellular system in the three-dimensional (3D) microenvironment, it remains unknown how the physical characteristics of individual cells regulate and coordinate tumour development and invasion.

By integrating confocal microscopy with optical tweezers, we have developed a platform to measure morphological characteristics, physical properties and migratory dynamics of individual cells throughout a growing multicellular 3D breast cancer model^{11,12}. By tracking the spatiotemporal evolution of individual cells during the growing process, we find heterogeneous patterns of cellular physical characteristics that facilitate tumour cell invasion. Compared with cells in the organoid core, those at the invasive leading edge are faster, softer and larger. The volumes of both the cell body and the nucleus are larger at the invasive leading edge, and the temporal fluctuations characterizing cytoplasmic dynamics become stronger. Blocking gap junctions (GJs) significantly suppresses these changes, suggesting that supracellular

fluid flow may drive the evolution of the observed patterns of cellular properties. Furthermore, the elimination of the softer subpopulation in the cancer organoid strongly delays the transition to an invasive phenotype. These findings highlight a causal role of spatiotemporal coordination of cellular physical properties—especially cell swelling and softening—in tumour development and invasive dynamics.

Epithelial cancer organoids have been widely used to model glandular epithelial cancers in 3D culture systems²⁸; these models recapitulate distinguishing physiological features of epithelial tissues and capture the pathological features of epithelial tumours. For example, the well-ordered epithelial architecture becomes disrupted, the lumen fills with cells and invasive branches then form²⁸. To reveal the mechanical underpinnings of this process, we transfected MCF 10A human breast epithelial cells with a green fluorescent protein (GFP) tagged with a nuclear-localization signal (NLS). We then seeded these cells into a 3D interpenetrating network hydrogel composed of 5 mg ml⁻¹ alginate and 4 mg ml⁻¹ Matrigel¹², with a shear modulus close to 300 Pa to mimic the mechanical microenvironment of a breast carcinoma in vivo^{12,29}.

Starting from a single cell, a multicellular cluster grows, and invasive branches develop over approximately 10 days (Fig. 1a–c); in accordance with recent definitions, we call this cluster a cancer organoid³⁰. During the early stage, an individual MCF 10A cell proliferates to form a spherical cluster (early stage; Fig. 1a, day 3). This cell cluster grows into a larger spheroid with cells both in the core and on the periphery (middle stage; Fig. 1b, day 5). As this spheroid develops further, invasive branches extend from the main body and invade the surrounding extracellular matrix (ECM) (later stage; Fig. 1c, day 10). The phenotype observed in this 3D breast cancer model shows uncontrolled cellular proliferation, lack of cellular polarization and the initiation of matrix invasion, much like those observed in vivo in invasive ductal carcinomas (Fig. 1d). This

¹Department of Mechanical Engineering, Massachusetts Institute of Technology, Cambridge, MA, USA. ²Department of Physics, University of Ottawa, Ottawa, Ontario, Canada. ³Harvard John A. Paulson School of Engineering and Applied Sciences, Cambridge, MA, USA. ⁴School of Systems Science, Beijing Normal University, Beijing, China. ⁵Key Laboratory of Soft Matter Physics, Institute of Physics, Chinese Academy of Sciences, Beijing, China. ⁶Xuanwu Hospital, Capital Medical University, Beijing, China. ⁷Harvard T. H. Chan School of Public Health, Boston, MA, USA. *e-mail: guom@mit.edu

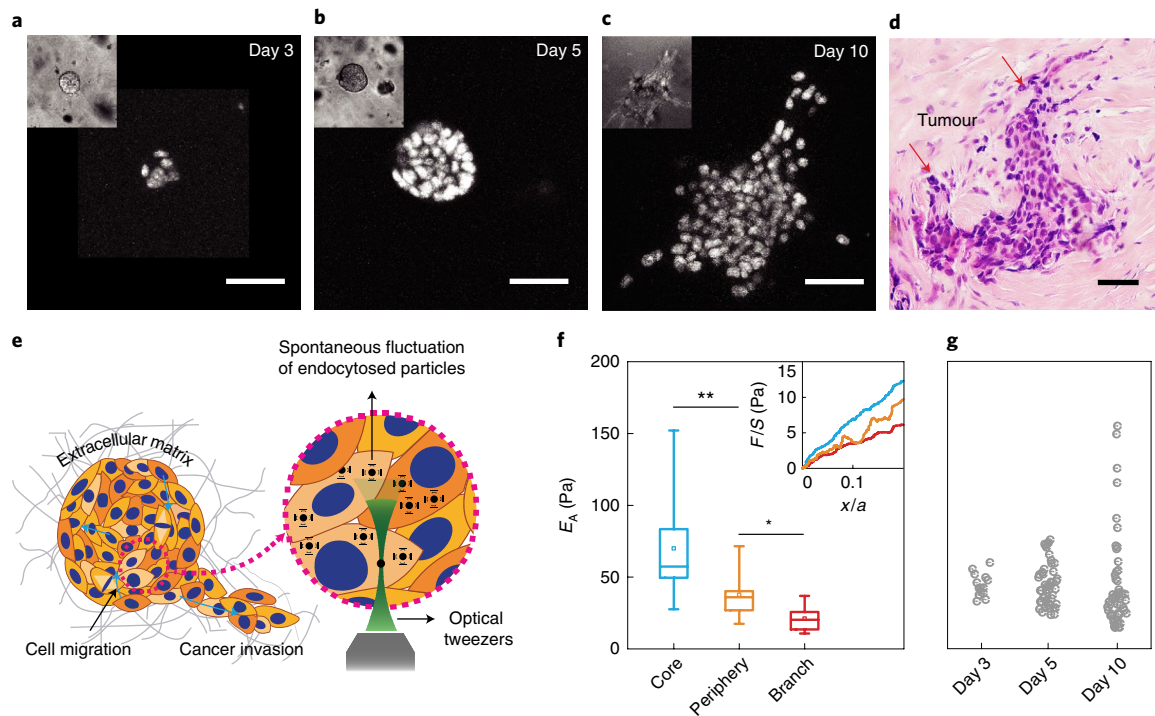


Fig. 1 | Evolution of heterogeneity and subpopulations of cell stiffness in the growing cancer organoid. a–c, Cross-section images of epithelial cancer organoid developed from GFP-NLS-labelled MCF 10A cells at different stages: early stage (day 3; **a**), middle stage (day 5; **b**) and later stage (day 10; **c**). **d,** Haematoxylin and eosin stains from grade-2 ER+ invasive ductal carcinoma human breast cancer tissue samples. Tumour glands are indicated using red arrows. **e,** Schematic of the cytoplasmic mechanics and dynamics measurements in a growing cancer organoid using optical tweezers. **f,** E_A of individual cells in the core, periphery and branch regions of the cancer organoid, quantified from slopes of the normalized force–displacement curves (inset). F and x are the resistant force and displacement of the trapped particle. S and a are the cross-section area and diameter of the particle. The boxes represent the interquartile range between the first and third quartiles, whereas the whiskers represent the 95% and 5% values, and the squares represent the average. **g,** Mechanical heterogeneity of individual cells within the cancer organoid at different stages (y axis shared with **f**). Measurements are taken in more than three independent cancer organoids for **f** and **g**. ** $P < 0.05$; ** $P < 0.01$, *** $P < 0.001$. Scale bars in **a–d**, 50 μm .

contrasts with a normal acinar structure that develops when cells are seeded in a soft matrix (Supplementary Fig. 1).

The molecular pathways that regulate the invasion process in this model system have been well studied^{11,12}, but the associated changes in the physical properties of cells remain largely unknown. To characterize cell mechanics in this growing epithelial cancer organoid, we used optical tweezers to perform active microrheology and thus measure the mechanical properties of the cytoplasm within individual cells. To do this, we mixed small particles (0.5 μm diameter) into the ECM that became endocytosed by individual constituent cells. These particles were dragged unidirectionally by optical tweezers at 0.5 $\mu\text{m s}^{-1}$ to obtain a force–displacement relationship in the cytoplasm (illustrated in Fig. 1e), which thus characterized the cytoplasmic stiffness within each cell³¹. This force–displacement relationship was found to vary spatially within the growing cancer organoid (Fig. 1f, inset). To compare different regions, we spatially segmented the cancer organoid into three different populations: core, periphery and branch. At early stages, only one population was evident. At middle stages, however, cells were classified as being in the core if they were within the inner 40% of the cancer organoid radius. After branches formed, a central spheroidal mass was defined and separated into core and periphery cells, with all other cells assigned to the branches (Supplementary Fig. 2a). We found that the force required to deform the cytoplasm of cells in the core of the cancer organoid was appreciably greater than that required for cells in the periphery or in a branch (Fig. 1f, inset). To further quantify this difference, we measured an apparent modulus E_A of the cytoplasm by taking the average slope of the linear regime of

the normalized force–displacement curve. We found that the cells in the core of the cancer organoid were the stiffest, while the cells in the branches were the softest (Fig. 1f). Moreover, the range of stiffness and the population heterogeneity increased as the cancer organoid developed (Fig. 1g), consistent with findings from in vivo samples, where increasing mechanical heterogeneity during disease progression has been observed³². This evolution from a homogeneous to heterogeneous population with distinct mechanical properties is reminiscent of the epigenetic heterogeneity that has been observed in breast tumour progression³³.

Given the spatial variation observed in cell stiffness, we wondered whether cytoplasmic dynamics also vary in different regions of the cancer organoid. To quantify cytoplasmic dynamics, we used confocal microscopy to image spontaneous fluctuations of endocytosed fluorescent particles (0.5 μm diameter), which are larger than the typical cytoskeletal mesh size (~ 50 nm); particle motions reflect the active non-equilibrium force fluctuations that spontaneously arise within the cytoplasm and thus also influence the dynamics of proteins and organelles in the cytoplasm²². By tracking trajectories of these particles, we calculated the time- and ensemble-averaged mean-squared displacement (MSD) $\langle \Delta r^2(\tau) \rangle$, where $\Delta r(\tau) = r(t+\tau) - r(t)$, r and τ represent the particle displacement and the lag time. When comparing the MSD for different regions of the cancer organoid, we found that the dynamics in the core were smallest, followed by those in the periphery cells, with branch cells showing the greatest cytoplasmic dynamics (Fig. 2a). Beyond cytoplasmic dynamics, we found similar differences in intranuclear dynamics; the diffusion of GFP in the cell nucleus, probed by

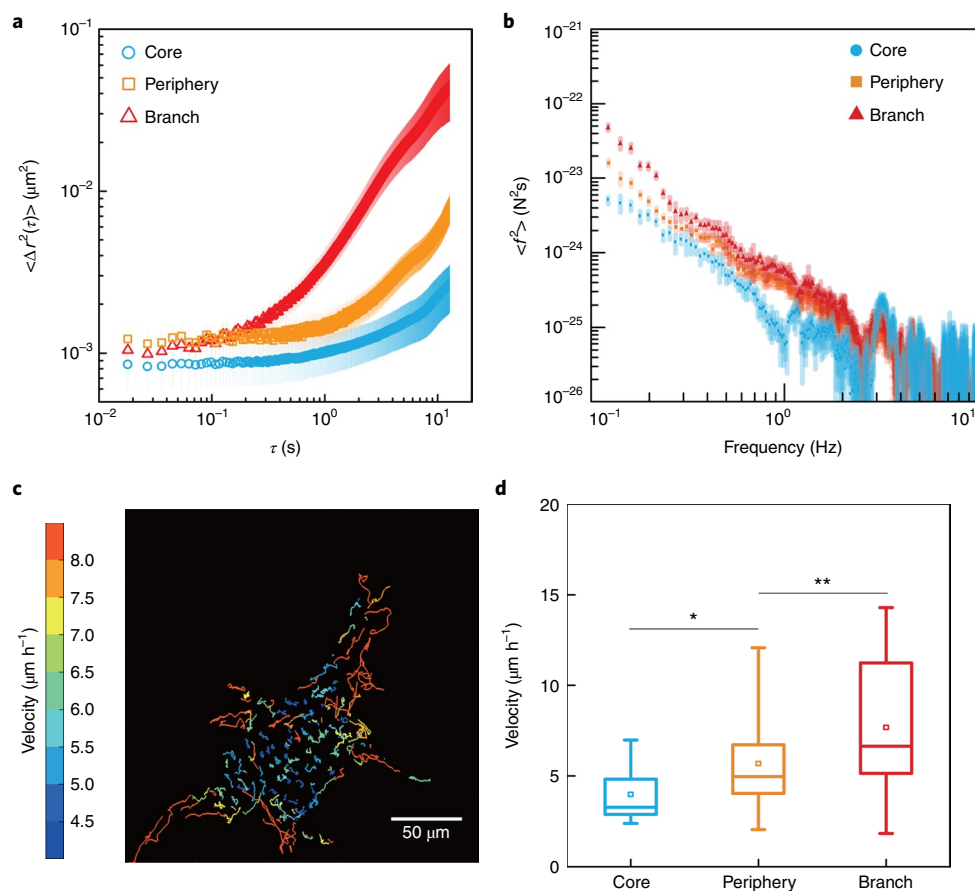


Fig. 2 | Different cell subpopulations in a cancer organoid show distinct dynamic behaviours. **a**, 2D time- and ensemble-averaged MSD of 0.5- μm -diameter particles are plotted against lag time on log-log axes, in the cytoplasm of cells in the core, periphery and branch regions of the cancer organoid. The data are averaged from 15 independent measurements, and the error bars represent ± 1 s.d. **b**, Cytoplasmic force spectrum $\langle f^2 \rangle$ calculated from spontaneous fluctuations of tracer particles and the active microrheology measurements through $\langle f^2(\omega) \rangle = |K(\omega)|^2 \langle r^2(\omega) \rangle$ inside cells at different locations of the cancer organoid. Data are shown as mean \pm standard deviation ($n > 10$). **c**, Cell migratory trajectories over 4 h reveal a highly dynamic scenario of cell migration within the central 20 μm cross-section of the cancer organoid. The colour scale indicates the average migratory speed of each cell. **d**, The migratory speed of cells in each subpopulation is plotted. The boxes represent the interquartile range between the first and third quartiles, whereas the whiskers represent the 95% and 5% values, and the squares represent the average. * $P < 0.05$; ** $P < 0.01$; *** $P < 0.001$.

fluorescent recovery after photobleaching, was also substantially slower in the core region compared with that in the periphery of the cancer organoid (Supplementary Fig. 2b,c).

While the change in intracellular dynamics was consistent with the changes in cytoplasmic stiffness, the dynamics are influenced not only by the passive mechanical properties of the cytoplasm but also by active ATP-dependent force fluctuations within the cell²². To measure the latter, we used force spectrum microscopy (FSM), which combines measurements of the spontaneous fluctuations of probe particles with the micromechanical measurement in the cytoplasm to quantify the spectrum of the aggregate force fluctuations $\langle f^2(\omega) \rangle$ in the cell, where f is the aggregate force in the cytoplasm and ω is the frequency; this force fluctuation spectrum reflects the total enzymatic activity²². Using FSM, we found that cells in the branch have the highest cytoplasmic force fluctuations, with magnitudes approximately five times greater at 1 Hz than those of cells in the spheroid core (Fig. 2b).

We also assessed cell motility by imaging the cancer organoid at a high spatial and temporal resolution. Full 3D images of the organoid were recorded by confocal microscopy every 10 min over a period of 24 h subsequent to a branch forming (Supplementary Videos 1 and 2). By tracking the position of every cell nucleus, cell tracks were constructed (Fig. 2c). From the cell tracks, the migration

speed of every cell in this 3D organoid was calculated. All cells were constantly migrating, but cells in the branches or in the periphery migrated faster than cells in the core (Fig. 2d). This spatial dependence in migration speed mirrored the spatial dependence of cytoplasmic dynamics.

Cell volume is another important physiological property that is known to correlate with cell stiffness and dynamics^{26,34}. To compare cell and nuclear volumes, we fluorescently labelled the whole cell using cytoplasmic staining (in addition to the already GFP-NLS-labelled cell nuclei) and measured volumes using 3D confocal microscopy. We found that over a wide range of organoid sizes, the ratio of nuclear to cell volume in individual cells remained constant ($13 \pm 1\%$, Supplementary Fig. 3), in agreement with previous findings^{26,35}, allowing us to measure nuclear volume in lieu of cell volume. At early stages of cancer organoid development, when no clear subregions existed, cells had similar nuclear volumes (Fig. 3a, day 3). As the organoid developed, nuclear volumes increased in spatial variability (Fig. 3a, days 5 and 10); the nuclear volume of the cells correlated strongly with the relative cell positions within the cancer organoid (Fig. 3b, days 5 and 10), with smaller cells in the core. The transition from the early to middle period of development led to cells in the core becoming systematically smaller (Fig. 3c, day 5). As growth continued, the cancer organoid eventually underwent

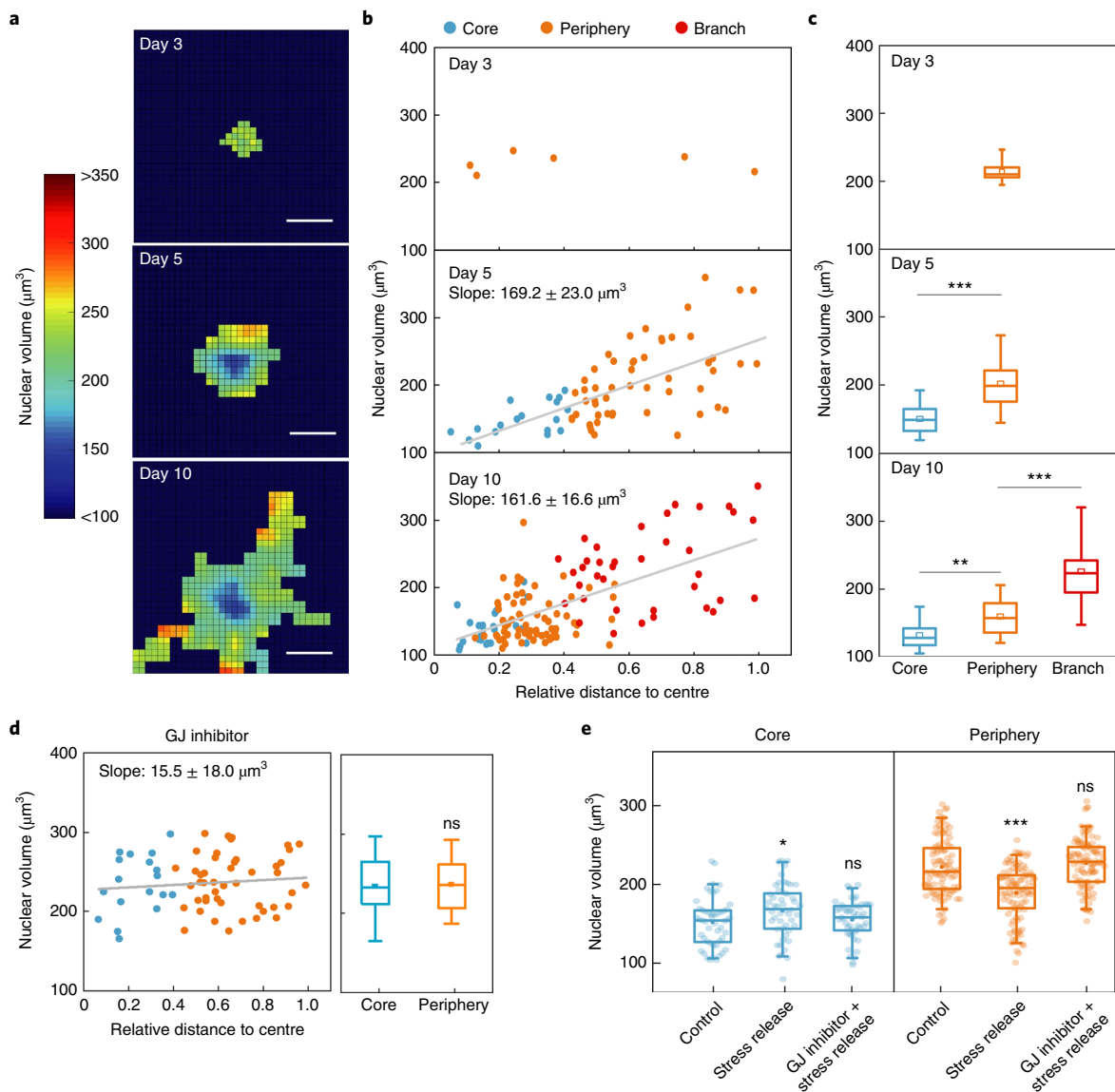


Fig. 3 | Temporal and spatial evolution of cell volume during the growth of cancer organoids. **a**, Nuclear volume heat map showing the evolution of cell nuclear volume distribution in the developing cancer organoid. Scale bars, 50 μm . **b**, The nuclear volume of every cell in the cancer organoid is plotted against the relative distance to the organoid centre at different stages, showing a strong correlation between nuclear volume and spatial position, especially at middle and later stages. **c**, Nuclear volume of cells in different geometrical regimes of the cancer organoids ($n > 3$). **d**, Nuclear volume of individual cells in GJ-inhibited cancer organoids. **e**, Stress release changes the distribution of individual nuclear volumes in the core and periphery if GJs are intact. The boxes represent the interquartile range between the first and third quartiles, whereas the whiskers represent the 95% and 5% values, and the squares represent the average. * $P < 0.05$; ** $P < 0.01$; *** $P < 0.001$; ns, not significant.

an invasive transition marked by the formation and growth of branches into the ECM. While the core and periphery still displayed clearly distinct nuclear volumes, the formation of invasive branches resulted in cells with even larger nuclear volumes (Fig. 3c, day 10). The nuclear volume of cells in the same regime also evolved as the cancer organoid grew; cell nuclei in the core became smaller as the size of the cancer organoid increased from days 5 to 10 (Fig. 3c, blue boxes). This spatial pattern of nuclear volume was also observed in other 3D mammary cancer models using different cell lines and ECMs, such as MCF 10A and MCF 10AT in the collagen–Matrigel system¹¹ (Supplementary Fig. 4).

GJs are specialized intercellular connections between epithelial cells and have been widely observed in normal and malignant breast tissues³⁶. They connect the cytoplasm of two neighbouring

cells, and thus allow molecules and ions to directly pass through^{37,38}. Accumulating evidence has shown that there is compressive stress within tumour tissue and 3D cancer models^{39–42}. Therefore, we hypothesize that the observed volume gradient in our system is a result of supracellular fluid flow through cell–cell GJs, driven by the higher intratumour compressive stress. To test whether the volume gradient is GJ-dependent, we added a GJ inhibitor (carbenoxolone⁴³, 500 μM) to our system on day 3, when the volume gradient was not yet present (Fig. 3a,b, day 3). As the cancer organoid continued to grow, we did not observe a significant difference in the nuclear volume of cells between those in the core and the periphery (Fig. 3d). Similar results were observed when we used a different type of GJ inhibitor, connexin mimetic peptides (CMPs)⁴⁴ (Supplementary Fig. 5). These results suggest that the GJs within

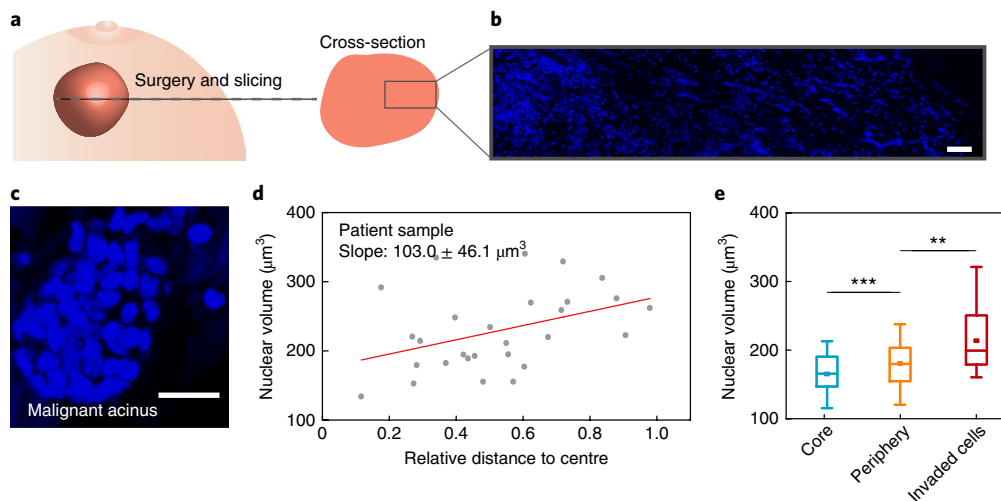


Fig. 4 | Characterization of cell volume heterogeneity in patient samples. **a**, Schematic of a tumour biopsy from a breast cancer patient. **b**, Large-scale fluorescent image showing cell nuclei from the core to the edge area of the biopsy. Scale bar, 50 μm . **c**, Invasive acinar structures within the biopsy. Scale bar, 20 μm . **d**, Individual cell nuclear volume is plotted against the cell's relative distance to the centre of the invasive acinar structure. **e**, Nuclear volume of cells in different geometrical regimes of the invasive acinar structures ($n = 3$). * $P < 0.05$; ** $P < 0.01$; *** $P < 0.001$.

the organoid play a role in the development of the observed cellular volume pattern. It has also been consistently shown that externally applied mechanical stress can drive fluid flow between cells through GJs in a two-dimensional (2D) monolayer⁴⁵ and in 3D MCF 10A clusters⁴⁶ to induce cell volume variations.

To investigate this hypothesis further, we tested whether the intratumour mechanical stress^{39–42} is a factor in the observed cell volume gradient. Using organoids cultured in a collagen–Matrigel network, we reduced the mechanical stresses on day 5 by releasing the organoids from the matrix confinement using collagenase. Six hours after stress release, we observed a significant increase in the cellular volume in the core and a decrease in cellular volume in the periphery (Fig. 3e, stress release). The initial cell volume gradient then became much weaker, suggesting an inverse supracellular fluid flow from the periphery to the core following stress release. To further test our hypothesis that GJs play a role in supracellular fluid flow, we blocked the GJs 6h before releasing the stress, and we did not observe any significant changes in cellular volume or cell volume gradient on stress release (Fig. 3e, ‘GJ inhibitor + stress release’). These results indicate that the imbalance of intratumour stress drives a fluid flow through GJs in the 3D cancer model system, which results in the swelling and shrinking of cells in the periphery and the core, respectively.

For both isolated cells and confluent monolayers in 2D, cell volume has been found to vary with cell stiffness and internal dynamics, with a decrease in cell volume corresponding to an increase in cell stiffness and a decrease in internal dynamics^{26,34}. Similar trends prevailed in the developing 3D cancer organoid. Cells in the core became smaller, stiffer and less dynamic. By contrast, cells in the branches became bigger, softer and more dynamic. When we tracked individual cell positions over time, we found that cells transit from the core to the periphery or vice versa (Supplementary Fig. 6a,b). Moreover, if we track a cell in a branch it tends to be swollen, but as it moves towards the core, it shrinks. The converse is true for tracking a cell in the core (Supplementary Fig. 6c,d); as a cell transits the cancer organoid, it adjusts its physical properties to its local microenvironment.

The responsiveness of cell volume to the local microenvironment raises the question of whether similar variability in cell volume exists in real tumour samples. To answer this question, we obtained grade-2 ER+ invasive ductal carcinoma human breast

cancer tissue samples from a patient, then fixed and sectioned each sample before staining and imaging them with confocal microscopy (Fig. 4a,b). Within the tumour mass, spheroidal, acinar clusters of cells surrounded by basement membrane were evident (Fig. 4c and Supplementary Video 3), which share similar characteristics with our 3D cancer model. In such spheroidal acinar clusters, we found that the nuclear volume increased as the distance from the centre increased (Fig. 4d), consistent with our model system. Cells in the core had smaller volumes, while invasive cells that appeared to have escaped from the main cluster had larger volumes (Fig. 4e).

These findings raise the interesting question of whether the swelling and softening of peripheral cells are important factors in invasive dynamics. To investigate this further, we artificially manipulated the stiffness and volume of peripheral cells. For example, we changed the osmotic pressure to either compress (with an additional 2% PEG300) or swell (with an additional 10% water) the cells on day 3, before the formation of various subpopulations (Fig. 5a–c). We also tried increasing cell stiffness using the chemotherapy medication daunorubicin (0.5 μM), jasplakinolide (5 μM)⁴⁷ or overexpression of actin crosslinking protein α -actinin. We found that the volume of cells in the periphery changed, while little change was observed in the core (Fig. 5f). The decrease or increase in cell volume was accompanied by a corresponding increase or decrease in cell stiffness (Fig. 5f). Long-term exposure to any of these interventions did not significantly impair cell proliferation; the projected area of individual growing cancer organoids increased over time in a fashion similar to those in the control medium (Fig. 5d). However, the invasion changed considerably compared with the control case, where invasiveness was quantified as the percentage of cancer organoids that formed invasive branches after 11 days in each sample, with softer peripheral cells leading to greater invasiveness (Fig. 5e, Supplementary Fig. 7). Furthermore, we used GJ inhibitors (carboxolone⁴³, 500 μM , or CMPs⁴⁴, 600 μM) to perturb the spontaneous cell swelling and softening process in our system on day 3 (Fig. 5f) and found that the invasion of the tumour cells was also delayed (Fig. 5e). To exclude the possibility that GJ inhibitors directly impact cell mechanics, we measured the cytoplasmic stiffness of isolated MCF 10A cells with GJ inhibitors on a 2D surface and found that the GJ inhibitors did not affect cytoplasmic stiffness (Supplementary Fig. 8). By controlling the volume and stiffness of

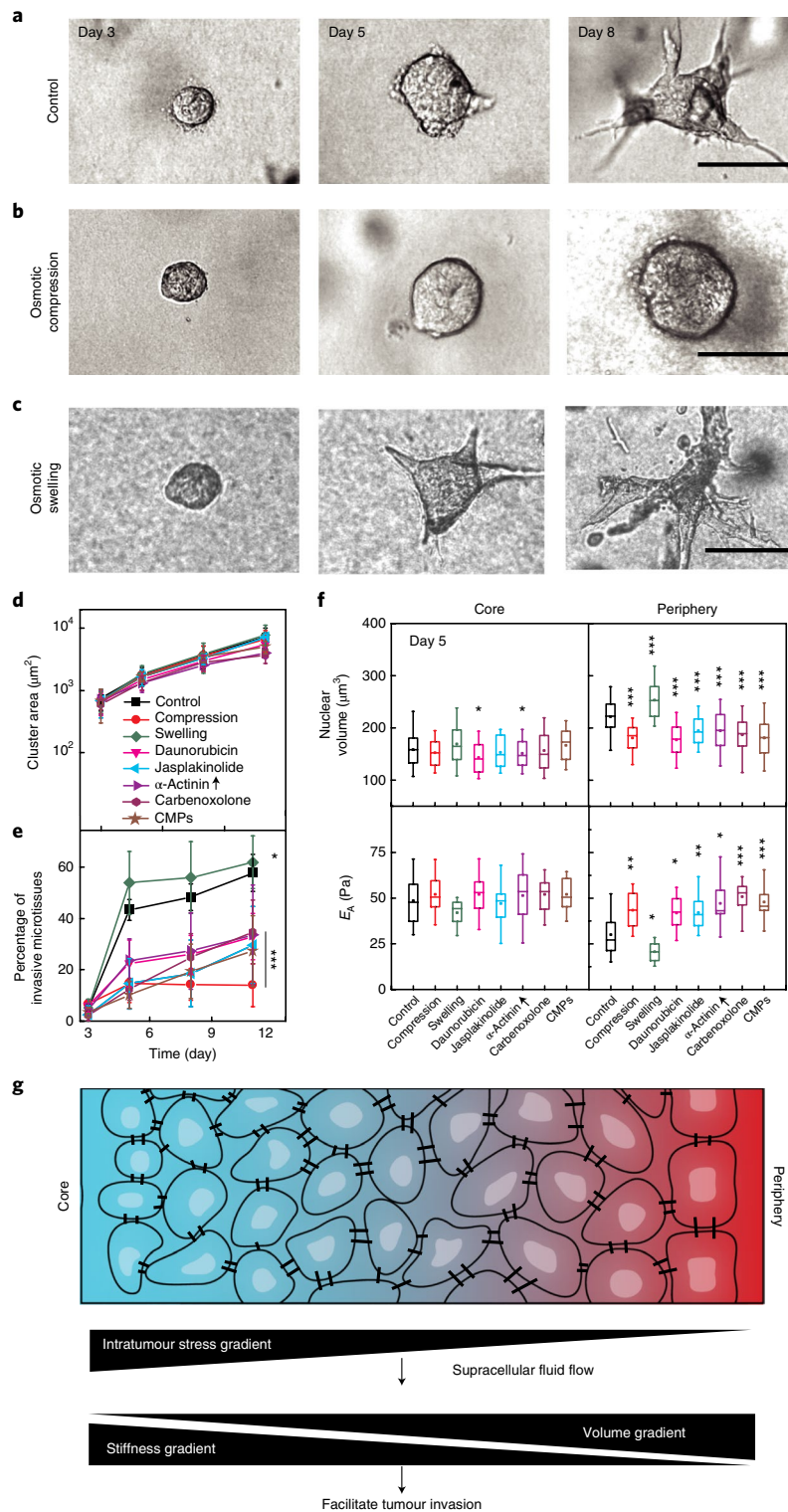


Fig. 5 | Stiffening the soft cell subpopulation inhibits the invasion of the tumour cells. a–c, Bright-field images showing the time-dependent morphological changes in the developing cancer organoids under different culture conditions, including complete culture medium (**a**), osmotic compression (**b**) and osmotic swelling (**c**). **d**, Quantification of the projected areas of cancer organoids shows that the growth rates under different culture conditions are comparable. **e**, Percentage of the invasive cancer organoids over time under different culture conditions. Asterisks indicates the statistically significant difference between each group and the control on day 11. **f**, Cell nuclear volume and cell stiffness in the core and periphery of the organoids under the different culture conditions in **d**. The boxes represent the interquartile range between the first and third quartiles, whereas the whiskers represent the 95% and 5% values, and the squares represent the average. **g**, Working hypothesis: the intratumour stress gradient drives supracellular fluid flow and thus results in cell volume and stiffness gradients, which together facilitate tumour cell invasion. Scale bars in **a–c**, 50 μm . Error bars in **d** and **e** indicate standard deviation. Measurements were taken in three independent experiments. * $P < 0.05$; ** $P < 0.01$; *** $P < 0.001$.

the peripheral cells, we significantly altered the invasive behaviour of our 3D cancer model.

An understanding of how mechanical changes in cells enable disease advancement is critical for determining how cancer progresses. The invasion of MCF 10A clusters has previously been shown to depend on ECM mechanics through PI3K activation^{11,12,48}; we indeed confirm that this is critical for disease initiation (Supplementary Figs. 9 and 10). However, after this initial stage of disease progression, we found that mechanical heterogeneity increased, giving rise to larger, softer cells and enhanced invasiveness. For isolated cells in the 3D culture, cell–matrix interactions can potentially lead to an increase in cell volume⁴⁹; this cannot be excluded from the factors that play a role in peripheral cells. Nonetheless, the inhibition of GJs interfered with cell volume change during growth and stress release, indicating that fluid flow across cell boundaries plays a role in mechanical pattern formation. The role of GJs in cancer progression is still under debate, with both promotion and suppression of invasiveness having been observed across various types of cancer and GJ⁵⁰. Our results hint at a purely physical mechanism by which GJs can affect cancer progression. A change in the water content of cells and hence the degree of molecular crowding^{26,34} will affect a wide range of downstream cell functions and properties. As such, our emerging physical picture of tumour progression now includes 3D spatiotemporal evolution of cellular physical properties.

Online content

Any methods, additional references, Nature Research reporting summaries, source data, statements of code and data availability and associated accession codes are available at <https://doi.org/10.1038/s41567-019-0680-8>.

Received: 21 September 2018; Accepted: 4 September 2019;
Published online: 21 October 2019

References

- Rigato, A., Miyagi, A., Scheuring, S. & Rico, F. High-frequency microrheology reveals cytoskeleton dynamics in living cells. *Nat. Phys.* **13**, 771–775 (2017).
- Fenz, S. F. et al. Membrane fluctuations mediate lateral interaction between cadherin bonds. *Nat. Phys.* **13**, 906–913 (2017).
- Tanimoto, H., Sallé, J., Dodin, L. & Minc, N. Physical forces determining the persistency and centring precision of microtubule asters. *Nat. Phys.* **14**, 848–854 (2018).
- Nam, S. & Chaudhuri, O. Mitotic cells generate protrusive extracellular forces to divide in three-dimensional microenvironments. *Nat. Phys.* **14**, 621–628 (2018).
- Serra-Picamal, X. et al. Mechanical waves during tissue expansion. *Nat. Phys.* **8**, 628–634 (2012).
- Ingber, D. E. et al. in *Mechanical Engineering of the Cytoskeleton in Developmental Biology* Vol. 150 (ed. Gordon, R.) 173–224 (Elsevier, 1994).
- Tambe, D. T. et al. Collective cell guidance by cooperative intercellular forces. *Nat. Mater.* **10**, 469–475 (2011).
- Xue, X. et al. Mechanics-guided embryonic patterning of neuroectoderm tissue from human pluripotent stem cells. *Nat. Mater.* **17**, 633–641 (2018).
- Karzbrun, E., Kshirsagar, A., Cohen, S. R., Hanna, J. H. & Reiner, O. Human brain organoids on a chip reveal the physics of folding. *Nat. Phys.* **14**, 515–522 (2018).
- Trepast, X. & Sahai, E. Mesoscale physical principles of collective cell organization. *Nat. Phys.* **14**, 671–682 (2018).
- Paszek, M. J. et al. Tensional homeostasis and the malignant phenotype. *Cancer Cell* **8**, 241–254 (2005).
- Chaudhuri, O. et al. Extracellular matrix stiffness and composition jointly regulate the induction of malignant phenotypes in mammary epithelium. *Nat. Mater.* **13**, 970–978 (2014).
- Paszek, M. J. & Weaver, V. M. The tension mounts: mechanics meets morphogenesis and malignancy. *J. Mammary Gland Biol.* **9**, 325–342 (2004).
- Kumar, S. & Weaver, V. M. Mechanics, malignancy, and metastasis: the force journey of a tumor cell. *Cancer Metast. Rev.* **28**, 113–127 (2009).
- Pogoda, K. et al. Compression stiffening of brain and its effect on mechanosensing by glioma cells. *New J. Phys.* **16**, 075002 (2014).
- Levental, K. R. et al. Matrix crosslinking forces tumor progression by enhancing integrin signaling. *Cell* **139**, 891–906 (2009).
- Stowers, R. S. et al. Matrix stiffness induces a tumorigenic phenotype in mammary epithelium through changes in chromatin accessibility. *Nat. Biomed. Eng.* <https://doi.org/10.1038/s41551-019-0420-5> (2019).
- Suresh, S. Biomechanics and biophysics of cancer cells. *Acta Mater.* **55**, 3989–4014 (2007).
- Guck, J. et al. Optical deformability as an inherent cell marker for testing malignant transformation and metastatic competence. *Biophys. J.* **88**, 3689–3698 (2005).
- Fritsch, A. et al. Are biomechanical changes necessary for tumour progression? *Nat. Phys.* **6**, 730–732 (2010).
- Xu, W. et al. Cell stiffness is a biomarker of the metastatic potential of ovarian cancer cells. *PLoS ONE* **7**, e46609 (2012).
- Guo, M. et al. Probing the stochastic, motor-driven properties of the cytoplasm using force spectrum microscopy. *Cell* **158**, 822–832 (2014).
- Koch, T. M., Münster, S., Bonakdar, N., Butler, J. P. & Fabry, B. 3D traction forces in cancer cell invasion. *PLoS ONE* **7**, e33476 (2012).
- Swaminathan, V. et al. Mechanical stiffness grades metastatic potential in patient tumor cells and in cancer cell lines. *Cancer Res.* **71**, 5075–5080 (2011).
- Gandalovičová, A. et al. Migrastatics—anti-metastatic and anti-invasion drugs: promises and challenges. *Trends Cancer* **3**, 391–406 (2017).
- Guo, M. et al. Cell volume change through water efflux impacts cell stiffness and stem cell fate. *Proc. Natl Acad. Sci. USA* **114**, E8618–E8627 (2017).
- Byfield, F. J., Reen, R. K., Shentu, T.-P., Levitan, I. & Gooch, K. J. Endothelial actin and cell stiffness is modulated by substrate stiffness in 2D and 3D. *J. Biomech.* **42**, 1114–1119 (2009).
- Debnath, J. & Brugge, J. S. Modelling glandular epithelial cancers in three-dimensional cultures. *Nat. Rev. Cancer* **5**, 675–688 (2005).
- Acerbi, I. et al. Human breast cancer invasion and aggression correlates with ECM stiffening and immune cell infiltration. *Integr. Biol.* **7**, 1120–1134 (2015).
- Simian, M. & Bissell, M. J. Organoids: a historical perspective of thinking in three dimensions. *J. Cell Biol.* **216**, 31–40 (2017).
- Hu, J. et al. Size- and speed-dependent mechanical behavior in living mammalian cytoplasm. *Proc. Natl Acad. Sci. USA* **114**, 9529–9534 (2017).
- Plodinec, M. et al. The nanomechanical signature of breast cancer. *Nat. Nanotechnol.* **7**, 757–765 (2012).
- McGranahan, N. & Swanton, C. Clonal heterogeneity and tumor evolution: past, present, and the future. *Cell* **168**, 613–628 (2017).
- Zhou, E. et al. Universal behavior of the osmotically compressed cell and its analogy to the colloidal glass transition. *Proc. Natl Acad. Sci. USA* **106**, 10632–10637 (2009).
- Jovtchev, G., Schubert, V., Meister, A., Barow, M. & Schubert, I. Nuclear DNA content and nuclear and cell volume are positively correlated in angiosperms. *Cytogenet. Genome Res.* **114**, 77–82 (2006).
- Teleki, I. et al. Correlations of differentially expressed gap junction connexins Cx26, Cx30, Cx32, Cx43 and Cx46 with breast cancer progression and prognosis. *PLoS ONE* **9**, e112541 (2014).
- Staelin, L. A. Three types of gap junctions interconnecting intestinal epithelial cells visualized by freeze-etching. *Proc. Natl Acad. Sci. USA* **69**, 1318–1321 (1972).
- Wade, M. H., Trosko, J. E. & Schindler, M. A fluorescence photobleaching assay of gap junction-mediated communication between human cells. *Science* **232**, 525–528 (1986).
- Dolega, M. et al. Cell-like pressure sensors reveal increase of mechanical stress towards the core of multicellular spheroids under compression. *Nat. Commun.* **8**, 14056 (2017).
- Lee, W. et al. Dispersible hydrogel force sensors reveal patterns of solid mechanical stress in multicellular spheroid cultures. *Nat. Commun.* **10**, 144 (2019).
- Mohagheghian, E. et al. Quantifying compressive forces between living cell layers and within tissues using elastic round microgels. *Nat. Commun.* **9**, 1878 (2018).
- Nia, H. T. et al. Solid stress and elastic energy as measures of tumour mechanopathology. *Nat. Biomed. Eng.* **1**, 0004 (2016).
- Manjarrez-Marmolejo, J. & Franco-Pérez, J. Gap junction blockers: an overview of their effects on induced seizures in animal models. *Curr. Neuropharmacol.* **14**, 759–771 (2016).
- Evans, W. H. & Boitano, S. Connexin mimetic peptides: specific inhibitors of gap-junctional intercellular communication. *Biochem. Soc. T.* **29**, 606–612 (2001).
- Zehnder, S. M. et al. Multicellular density fluctuations in epithelial monolayers. *Phys. Rev. E* **92**, 032729 (2015).
- McLachlan, E., Shao, Q., Wang, H.-I., Langlois, S. & Laird, D. W. Connexins act as tumor suppressors in three-dimensional mammary cell organoids by regulating differentiation and angiogenesis. *Cancer Res.* **66**, 9886–9894 (2006).
- Schulze, C. et al. Stiffening of human skin fibroblasts with age. *Biophys. J.* **99**, 2434–2442 (2010).
- Rubashkin, M. G. et al. Force engages vinculin and promotes tumor progression by enhancing PI3K activation of phosphatidylinositol (3, 4, 5)-triphosphate. *Cancer Res.* **74**, 4597–4611 (2014).

49. Lee, H.-p, Stowers, R. & Chaudhuri, O. Volume expansion and TRPV4 activation regulate stem cell fate in three-dimensional microenvironments. *Nat. Commun.* **10**, 529 (2019).
50. Aasen, T., Mesnil, M., Naus, C. C., Lampe, P. D. & Laird, D. W. Gap junctions and cancer: communicating for 50 years. *Nat. Rev. Cancer* **16**, 775–788 (2016).

Acknowledgements

This work was supported by National Cancer Institute grant no. 1U01CA202123. J.J.F. is also supported by National Institute of Health grant nos. R01HL148152 and PO1HL120839. M.G. also acknowledges support from the Department of Mechanical Engineering at the Massachusetts Institute of Technology.

Author contributions

Y.L.H. and M.G. designed the experiments. M.G. supervised the project. Y.L.H., H.L., Z.G., K.L., H.K., Y.Y., Y.L., W.T. and L.T. performed the experiments. Y.L.H., A.F.P., G.X., Z.G., J.S., Y.H. and S.K.G. developed MATLAB scripts for image processing and

data analysis. Y.L.H., A.F.P., J.J.F. and M.G. wrote the manuscript. All authors edited and approved the manuscript.

Competing interests

The authors declare no competing interests.

Additional information

Supplementary information is available for this paper at <https://doi.org/10.1038/s41567-019-0680-8>.

Correspondence and requests for materials should be addressed to M.G.

Reprints and permissions information is available at www.nature.com/reprints.

Publisher's note Springer Nature remains neutral with regard to jurisdictional claims in published maps and institutional affiliations.

© The Author(s), under exclusive licence to Springer Nature Limited 2019

Methods

Cancer organoid culture and immunofluorescence staining. The mammary epithelial cancer organoid with invasive phenotype was cultured and induced following a previously established protocol^{11,12}. Briefly, MCF 10A cells (ATCC) were cultured in a DMEM/F12 medium (Invitrogen, 11965-118) supplemented with 5% horse serum (Invitrogen, 16050-122), 20 ng ml⁻¹ epidermal growth factor (Peprotech, AF-100-15), 0.5 μg ml⁻¹ hydrocortisone (Sigma, H-0888), 100 ng ml⁻¹ cholera toxin (Sigma, C-8052), 10 μg ml⁻¹ insulin (Sigma, I-1882) and 1% penicillin and streptomycin (Thermo Fisher, 15140122). The cells were collected using a 0.05% trypsin-EDTA solution (Thermo Fisher, 25300054) after they reached confluence within T-25 flasks in a normal cell culture incubator and were mixed with the gel precursor solution at a low cell concentration (10⁴ ml⁻¹) to avoid interaction between cancer organoids. For alginate–Matrigel interpenetrating network hydrogels, the gel was composed of alginate (FMC Biopolymer) and Matrigel (Corning, 354234) with final concentrations of 5 mg ml⁻¹ and 4 mg ml⁻¹, respectively. The gel precursor with cells was put in the cell culture incubator for gelation. After 1 h, an additional complete culture medium was added to keep the gel hydrated. Cancer organoids developed in the 3D gels in the following ~10 days. For the collagen–Matrigel system, the gel was composed of 3.5 mg ml⁻¹ collagen and 0.5 mg ml⁻¹ Matrigel. The MCF 10AT cell line was a gift from J. Nickerson at the University of Massachusetts Medical School and was cultured under the same conditions as the MCF 10A cell line.

For immunohistochemical staining, the cancer organoids were cultured from normal MCF 10A cells (without GFP-NLS). The 3D gel with embedded cancer organoids was fixed with 4% paraformaldehyde at room temperature for 30 min. To increase the permeability of the cell membrane, the gel was immersed in PBS supplied with 0.2% Triton-X100 (2 h, room temperature). The sample was then blocked with 0.5% BSA in PBS for 5 h at room temperature and subsequently incubated overnight at 4 °C with primary antibodies for Cytokeratin 8 (1:300 diluted in PBS; Santa Cruz Biotechnology, sc-8020), Cytokeratin 14 (1:300 diluted in PBS; Santa Cruz Biotechnology, sc-53253), Phospho-Akt (1:200 diluted in PBS; Cell Signaling, 9271T), β-catenin (1:300 diluted in PBS; Santa Cruz Biotechnology, sc-7963), Integrin β4 (1:300 diluted in PBS; Santa Cruz Biotechnology, sc-13543) or laminin-5 (1:300 diluted in PBS; Santa Cruz Biotechnology, sc-13587). Corresponding secondary antibodies were added and incubated for another night at 4 °C (1:800; Thermo Fisher, A-11001 or A-11008). Finally, 4,6-diamidino-2-phenylindole (Thermo Fisher, D1306) was added for another 4 h to stain the cell nuclei. After each step, the samples were washed with PBS for at least 6 h.

Optical tweezer measurement. The laser beam (10 W, 1,064 nm) was tightly focused through a series of Keplerian beam expanders and a high numerical aperture objective (×100, 1.45, oil, Nikon). A high-resolution quadrant detector was used for position detection. To measure the mechanical properties of the cytoplasm, 0.5-μm-diameter latex particles (Sigma, L3280) were embedded in the gel and were endocytosed by the cells as they grew into cancer organoids. The linear regions of the detector and the trap stiffness were calibrated with the same bead using an active power-spectrum method and the equipartition theorem^{31,51,52}. The endocytosed bead was dragged at a constant velocity of 0.5 μm s⁻¹ by the optical trap, and the force–displacement curve of the local cytoplasm was recorded. To calculate E_A , the force and displacement were normalized by the cross-section area and the diameter of the particle, respectively. The slope in the linear range of the normalized force–displacement curve was taken as the E_A .

FSM. FSM combines measurements of the spontaneous fluctuation of probe particles with the micromechanical measurement in the cytoplasm to quantify the spectrum of $\langle f^2(\omega) \rangle$ in the cell, which in turn reflects total enzymatic activity²². To measure the spontaneous fluctuation of the cytoplasm, 0.5-μm-diameter fluorescent particles (Sigma, L5530) were embedded in the gel and were endocytosed by the cells as they grew into cancer organoids. The motions of the particles within the cytoplasm were recorded with a 10 ms interval using confocal microscopy. Particle centres were determined in each frame, and the trajectories of particles were obtained by minimizing the overall displacement between consecutive frames as demonstrated previously^{22,53} using a customized particle tracking algorithm. Time- and ensemble-averaged values of MSD were then calculated. The force spectrum was calculated using $\langle f^2(\omega) \rangle = |K(\omega)|^2 \langle r^2(\omega) \rangle$, where $\langle r^2(\omega) \rangle$ was obtained through the Fourier transform of MSD and the cytoplasmic spring constant $K(\omega)$ was obtained from the optical tweezer measurement with a power law assumption $K(\omega) = K(\omega = 1 \text{ Hz})\omega^\beta$, with $\beta = 0.15$ (refs. ^{22,54}).

Cell dynamics within the growing cancer organoid. To track the movement of individual cells, cancer organoids of GFP-NLS-labelled cells at different stages (days 3, 5 and 10) were imaged every 10 min for 24 h in a customized incubator (5% CO₂, 37 °C, 95% humidity) on a confocal microscope (Leica, TCL SP8). The 3D positions of cell nuclei were determined at each frame, and the trajectory of each cell was determined using the same particle-tracking method and algorithm as described above. The velocity of the cells can be calculated from the adjacent positions on the trajectory of each cell.

Cell and nuclear volume measurements. To visualize the cell nucleus, the MCF 10A cell line was transfected with GFP-NLS using lentivirus (Essen Bioscience, 4475). Stable cell lines were selected in a puromycin-containing culture medium (0.4 mg ml⁻¹; Thermo Fisher, A1113802). To study the volume evolution during the growth of the cancer organoid, cancer organoids were formed in the hydrogel and cultured in a customized incubator (5% CO₂, 37 °C, 95% humidity) on a confocal microscope. The 3D conformation of the cancer organoid was recorded every 6 h for 2 weeks. The 3D structure of each cell nucleus within a cancer organoid was reconstructed, and the nuclear volume was calculated by counting the voxels contained within the 3D structure using a customized algorithm in MATLAB (2017a). Deconvolution (HUYGENS software) was applied to the image before we calculated the volume, which helps improve the z resolution of traditional confocal microscopy. To estimate the error in the volume calculation from anisotropic resolution of the confocal microscope, we repeated our volume measurements using stimulated emission depletion microscopy with a super-resolution mode in the z direction (~250 nm), which is similar to the resolution in the x – y plane, to provide an isotropic volume reconstruction. We found a consistent volume pattern, as shown in Supplementary Fig. 11a. We also imaged the same cancer spheroid with both confocal microscopy and the super-resolution mode in stimulated emission depletion microscopy; we compared the cell volume measurement of each cell with these two methods and found consistent results (Supplementary Fig. 11b).

To calculate the distance from a cell to the centre of the cancer organoid, the centre of each cell was determined by locating the local intensity maximum within the nucleus, and the centre of the cancer organoid was calculated as the geometric centre of the shape formed by all of the cells. Cells were classified as being in the core if they were within the inner 40% of the cancer organoid radius at middle stage. After branches formed, a central spheroidal mass was defined and separated into core and periphery cells, with all other cells assigned to the branches. Using this geometrical categorization, the cell nuclear volume distribution is consistent with the results using molecular signatures as metric⁵⁵, as shown in Supplementary Fig. 12. To obtain the nuclear volume heat map, we projected each cell from a 20-μm-thick section at the middle plane of the cancer organoid into the x – y plane, and the nuclear volume at each location (6.5 μm × 6.5 μm grids on the x – y plane) was obtained by averaging the nuclear volumes of all cells going through this particular location during a 2 h window. To measure the cell volume, the GFP-NLS-expressing MCF 10A cells were incubated with cell-tracker deep-red dye (Thermo Fisher, C34565) and were mixed with non-fluorescent cells (those without cell-tracker red) to make the individual fluorescent cells distinguishable from their neighbours within the formed cancer organoid; these cancer organoids for cell volume measurement were formed using a poly(ethylene glycol)-based microwell. The 3D morphology of both the nucleus and cell body were then imaged with confocal microscopy, and volumes were calculated with the same algorithm in MATLAB.

Human tissue. Human tissue samples, including the normal breast tissue and tumour tissue, were obtained at the Xuanwu Hospital in Beijing, China, with the pre-approval of the Institutional Review Board. Invasive ductal carcinoma samples were obtained from patients undergoing surgical removal. The pathologically normal breast tissue was obtained 2 cm away from the tumour lesions in the same patient. Informed consent or assent was obtained from all patients and/or their parent or legal guardian. To measure the nuclear volume within surgical tumour samples, these samples were sectioned and fixed with 4% paraformaldehyde for 1 h. The central section crossing the tumour mass centre was then stained with Hoechst 33342 (Sigma, 14533) for 1 h to visualize cell nuclei and washed three times with PBS. The 3D structure of the tumour slice was imaged with confocal microscopy and the volume was calculated as described above. To exclude the lymphocytes from the analysis, we labelled the pan-cytokeratin (a common epithelial cell maker for humans; Thermo Fisher, MA5-13156) in patient samples using antibodies and found that the tumour tissue indeed contains many pan-cytokeratin-negative cells, which suggests non-cancer cells (Supplementary Fig. 13a). However, we rarely find lymphocytes near the invasive acinar-like structures, and almost all of the cells within the structure are positive for pan-cytokeratin (Supplementary Fig. 13b).

Mechanical and chemical perturbations. For osmotic compression experiments, PEG (300 MW; Sigma, 90878) was added to complete the culture media with a final concentration of 2% (v/v) either on day 3 (long-term) or day 5 (short-term). To record the growth of the cancer organoids in the long-term experiments, we frequently recorded bright-field images of cancer organoids for the 10 days following osmotic compression, and the areas of the cancer organoids were quantified using IMAGEJ (1.52e). To study the effect of osmotic compression on cell nuclear volume and cell stiffness within the cancer organoid, we took high-resolution 3D images before and after a 12 h osmotic compression, and the cell nuclear volume and stiffness were analysed as described above. Alternatively, we added common drugs, including 0.5 μM daunorubicin (Sigma, D8809) or 5 μM jaspalinolide (Santa Cruz Biotechnology, sc-202191), or overexpressed α-actinin (Addgene, 54975) using Lipofectamine 3000 (Thermo Fisher, L3000001) on day 3 to increase the stiffness of the cells within cancer

organoids. The growth of cancer organoids was recorded for 10 days. To investigate the effect of osmotic compression on organoid proliferation and apoptosis, we performed immunostaining of Ki67 (Cell Signaling, 9129S) and caspase-3 (Thermo Fisher, C10423) and found that these interventions did not affect cell proliferation or induce apoptosis in our system (Supplementary Fig. 14). To investigate the role of the PI3K pathway in the evolution of the cellular physical properties during the growing of the cancer organoid, we added 20 μM LY294002 (Sigma, L9908) to inhibit PI3K on day 3, and the growth of the cancer organoids was recorded for 10 days thereafter. The cell nuclear volume and stiffness were measured on day 10. To block the GJ communication between neighbouring cells within the cancer organoids, either 500 μM carbenoxolone (Sigma, C4790) or a mixture of (37,43)Gap 27 (300 μM ; Anaspec Inc., AS-62642) and (40)Gap 27 (300 μM ; Anaspec Inc., AS-62642) connexin mimetic peptides was added on day 3.

Statistics. A two-tailed Student's *t*-test was used when comparing the difference between two groups. For comparison between multiple groups, one-way analysis of variance with the Tukey method was used. In all cases, * $P < 0.05$; ** $P < 0.01$; *** $P < 0.001$; ns, not significant. In all box plots, the boxes represent the interquartile range between the first and third quartiles, whereas the whiskers represent the 95% and 5% values, and the squares represent the average.

Reporting Summary. Further information on research design is available in the Nature Research Reporting Summary linked to this article.

Data availability

Data supporting the findings of this study are available within the article and the Supplementary Information and Source Data and from the corresponding author on reasonable request.

Code availability

MATLAB scripts used in this work are available from the corresponding author on reasonable request.

References

51. Han, Y. L. et al. Cell contraction induces long-ranged stress stiffening in the extracellular matrix. *Proc. Natl Acad. Sci. USA* **115**, 4075–4080 (2018).
52. Hu, J. et al. High stretchability, strength, and toughness of living cells enabled by hyperelastic vimentin intermediate filaments. *Proc. Natl Acad. Sci. USA* **116**, 17175–17180 (2019).
53. Crocker, J. C. & Grier, D. G. Methods of digital video microscopy for colloidal studies. *J. Colloid Interf. Sci.* **179**, 298–310 (1996).
54. Gupta, S. K. & Guo, M. Equilibrium and out-of-equilibrium mechanics of living mammalian cytoplasm. *J. Mech. Phys. Solids* **107**, 284–293 (2017).
55. Mekhdjian, A. H. et al. Integrin-mediated traction force enhances paxillin molecular associations and adhesion dynamics that increase the invasiveness of tumor cells into a three-dimensional extracellular matrix. *Mol. Biol. Cell* **28**, 1467–1488 (2017).

Reporting Summary

Nature Research wishes to improve the reproducibility of the work that we publish. This form provides structure for consistency and transparency in reporting. For further information on Nature Research policies, see [Authors & Referees](#) and the [Editorial Policy Checklist](#).

Statistical parameters

When statistical analyses are reported, confirm that the following items are present in the relevant location (e.g. figure legend, table legend, main text, or Methods section).

n/a | Confirmed

- The exact sample size (n) for each experimental group/condition, given as a discrete number and unit of measurement
- An indication of whether measurements were taken from distinct samples or whether the same sample was measured repeatedly
- The statistical test(s) used AND whether they are one- or two-sided
Only common tests should be described solely by name; describe more complex techniques in the Methods section.
- A description of all covariates tested
- A description of any assumptions or corrections, such as tests of normality and adjustment for multiple comparisons
- A full description of the statistics including central tendency (e.g. means) or other basic estimates (e.g. regression coefficient) AND variation (e.g. standard deviation) or associated estimates of uncertainty (e.g. confidence intervals)
- For null hypothesis testing, the test statistic (e.g. F , t , r) with confidence intervals, effect sizes, degrees of freedom and P value noted
Give P values as exact values whenever suitable.
- For Bayesian analysis, information on the choice of priors and Markov chain Monte Carlo settings
- For hierarchical and complex designs, identification of the appropriate level for tests and full reporting of outcomes
- Estimates of effect sizes (e.g. Cohen's d , Pearson's r), indicating how they were calculated
- Clearly defined error bars
State explicitly what error bars represent (e.g. SD, SE, CI)

Our web collection on [statistics for biologists](#) may be useful.

Software and code

Policy information about [availability of computer code](#)

Data collection

The particle tracking (cells and particles within the cytoplasm) and volume calculation are processed with customized codes in Matlab. All codes are available upon request.

Data analysis

OriginLab 8.0 and Matlab 2016b are used to analyze the data in this study.

For manuscripts utilizing custom algorithms or software that are central to the research but not yet described in published literature, software must be made available to editors/reviewers upon request. We strongly encourage code deposition in a community repository (e.g. GitHub). See the Nature Research [guidelines for submitting code & software](#) for further information.

Data

Policy information about [availability of data](#)

All manuscripts must include a [data availability statement](#). This statement should provide the following information, where applicable:

- Accession codes, unique identifiers, or web links for publicly available datasets
- A list of figures that have associated raw data
- A description of any restrictions on data availability

The datasets generated during and/or analysed during the current study are available from the corresponding author on reasonable request.

Field-specific reporting

Please select the best fit for your research. If you are not sure, read the appropriate sections before making your selection.

Life sciences Behavioural & social sciences Ecological, evolutionary & environmental sciences

For a reference copy of the document with all sections, see [nature.com/authors/policies/ReportingSummary-flat.pdf](https://www.nature.com/authors/policies/ReportingSummary-flat.pdf)

Life sciences study design

All studies must disclose on these points even when the disclosure is negative.

Sample size	Five to fifteen microtumors are measured in each experiment. The precise number used are given in the figure legend.
Data exclusions	For imaging process, only clusters started from a single cell were examined to synchronize the growth of the clusters. To avoid the effects from other clusters, clusters that have close neighbor clusters were also excluded.
Replication	All the measurements were done at least in three independent experiments to verify the reproducibility of the experimental findings (precise number are given in the figure legend), and the results were consistent.
Randomization	Analyzed microtumors are randomly chosen.
Blinding	The investigators were blinded to group allocation during data collection and analysis for osmotic pressure and drug perturbation results.

Reporting for specific materials, systems and methods

Materials & experimental systems

n/a	Involved in the study
<input checked="" type="checkbox"/>	<input type="checkbox"/> Unique biological materials
<input type="checkbox"/>	<input checked="" type="checkbox"/> Antibodies
<input type="checkbox"/>	<input checked="" type="checkbox"/> Eukaryotic cell lines
<input checked="" type="checkbox"/>	<input type="checkbox"/> Palaeontology
<input checked="" type="checkbox"/>	<input type="checkbox"/> Animals and other organisms
<input type="checkbox"/>	<input checked="" type="checkbox"/> Human research participants

Methods

n/a	Involved in the study
<input checked="" type="checkbox"/>	<input type="checkbox"/> ChIP-seq
<input checked="" type="checkbox"/>	<input type="checkbox"/> Flow cytometry
<input checked="" type="checkbox"/>	<input type="checkbox"/> MRI-based neuroimaging

Antibodies

Antibodies used

Cytokeratin Pan Type I/II Antibody Cocktail (Thermo Fisher scientific, Catalog # MA5-13156)
 Cytokeratin 8 (Santa Cruz Biotechnology, sc-8020)
 Cytokeratin 14 (Santa Cruz Biotechnology, sc-53253)
 Phospho-Akt (Cell Signaling, 9271T)
 β -catenin (Santa Cruz Biotechnology, sc-7963)
 Integrin β 4 (Santa Cruz Biotechnology, sc-13543)
 laminin-5 (Santa Cruz Biotechnology, sc-13587)
 Alexa Fluor 488 goat anti-mouse IgG (H+L) (Thermo Fisher scientific, Catalog # A-11001)
 Alexa Fluor 647 goat anti-rat IgG (H+L) (Thermo Fisher scientific, Catalog # A-21247)

Validation

Cytokeratin Pan Type I/II Antibody Cocktail: <https://www.thermofisher.com/antibody/product/Cytokeratin-Pan-Type-I-II-Antibody-clone-AE1-AE3-Cocktail/MA5-13156>
 Cytokeratin 8: <https://www.scbt.com/scbt/product/cytokeratin-8-antibody-c51>
 Cytokeratin 14: <https://www.scbt.com/scbt/product/cytokeratin-14-antibody-ll001>
 Phospho-Akt: <https://www.cellsignal.com/products/primary-antibodies/phospho-akt-ser473-antibody/9271>
 β -catenin: <https://www.scbt.com/scbt/product/beta-catenin-antibody-e-5>
 Integrin β 4: <https://www.scbt.com/scbt/product/integrin-beta4-antibody-a9>
 laminin-5: <https://www.scbt.com/scbt/product/laminin-5-antibody-p3e4>
 Alexa Fluor 488 goat anti-mouse IgG (H+L): <https://www.thermofisher.com/antibody/product/Goat-anti-Mouse-IgG-H-L-Cross-Adsorbed-Secondary-Antibody-Polyclonal/A-11001>
 Alexa Fluor 647 goat anti-rat IgG (H+L) :<https://www.thermofisher.com/antibody/product/Goat-anti-Rat-IgG-H-L-Cross-Adsorbed-Secondary-Antibody-Polyclonal/A-21247>

Eukaryotic cell lines

Policy information about [cell lines](#)

Cell line source(s)

The MCF10A cell line was purchased from ATCC. MCF10AT cell line is a gift from Jeffrey Nickerson at University of Massachusetts Medical School.

Authentication

MCF10A cell line was freshly brought from ATCC (ATCC® CRL-10317™). We did not perform authentication for the MCF10AT cell line.

Mycoplasma contamination

MCF10A cell line tested negative for mycoplasma contamination by ATCC. We did not perform testing for MCF10AT cell line.

Commonly misidentified lines
(See [ICLAC](#) register)

No cell line listed by ICLAC was used.

Human research participants

Policy information about [studies involving human research participants](#)

Population characteristics

A 44-year-old female was diagnosed with grade-2 ER+ invasive-ductal-carcinoma on the left side breast.

Recruitment

The biopsy was obtained during the surgical treatment of the patient. Details are described in the Method of the paper.